Experimental, theoretical, and modelling investigation of the gas-phase reaction between the amidogen radical (NH_2) and acetaldehyde (CH_3CHO) at low temperatures

Kevin M. Douglas[a*], Lok Hin Desmond Li [a], Catherine Walsh[b], Julia H. Lehman[c], Mark A. Blitz[a,d], Dwayne E. Heard[a*]

[a]*School of Chemistry, University of Leeds, Leeds, LS2 9JT, UK*

[b]*School of Physics and Astronomy, University of Leeds, Leeds, LS2 9JT, UK*

[c]*School of Chemistry, University of Birmingham, Edgbaston, B15 2TT, UK*

[d]*National Centre for Atmospheric Science (NCAS), University of Leeds, Leeds, LS2 9JT, UK*

[*]corresponding authors. Email: k.m.douglas@leeds.ac.uk; d.e.heard@leeds.ac.uk

Supplementary Information

Introduction

S1. A brief introduction to the low-temperature kinetics of gas-phase reactions, to the astrochemistry of acetamide, and to the related reaction between NH_2 and formaldehyde.

An active field of astrochemical research remains the understanding of the reaction mechanisms for the formation of complex organic molecules (COMs), which are molecules observed in space containing carbon with at least 6 atoms.[4] Since the early 1960s, the development of ground based radio astronomy has led to a rapid rate of detection of COMs with a wide range of functional groups in the interstellar medium (ISM).[5] The detection of COMs at very high spatial resolution in cold objects suggests a gas-phase route to their formation rather than just *via* a pure surface-grain chemistry mechanism.[6] However, the mechanisms for forming many gas-phase COMs are still unknown, with both gas-phase and grain-surface (*via* non-thermal desorption) routes possible.

Many gas-phase reactions leading either to the removal or formation of COMs possess an activation barrier on their potential energy surface, and the Arrhenius equation $k = A \exp(-E_a/RT)$ would suggest a rate coefficient, k, which becomes vanishingly small at the very low temperatures encountered in interstellar environments. However, in our laboratory, we have discovered that for a significant number of reactions of OH with oxygenated organic compounds that contain activation barriers, k can increase dramatically at very low temperatures.[7-8] The explanation is the formation of a weakly-bound (~5-30 kJ mol^{-1}) hydrogen-bonded complex in the entrance channel to the reaction before the transition state (TS), which is sufficiently long-lived to undergo quantum mechanical tunnelling to form products. At sufficiently low temperatures the rate of dissociation of the pre-reaction complex (PRC) back to reactants becomes sufficiently small that the probability of quantum mechanical tunnelling to products under the barrier becomes much higher. The first and most studied example of this behaviour is the gas-phase reaction of OH with methanol, for which there are now several experimental kinetics studies at very low temperatures down to 11.7 K,[8-12] as well as theoretical calculations of the rate coefficients.[12-14] The reaction proceeds *via* abstraction of a hydrogen atom at either the methyl (to form CH_2OH) or the hydroxyl site (to form CH_3O), with activation barriers of 4.2 and 15.0 kJ mol^{-1}, respectively. The PRC is calculated to be bound by 20.5 kJ mol^{-1}, and a rapid increase in the rate coefficient was measured below 200 K, with k(22K)/k(200 K) ~100, a trend which could be reproduced with some success using reaction rate theory.[10, 13-15] The CH_3O product was observed experimentally, providing direct evidence for the mechanism, and formed via tunnelling under the higher barrier, consistent with theory which calculated a much higher imaginary frequency for the tunnelling motion to form CH_3O compared to forming CH_2OH. Astronomical abundances of the methoxy radical, CH_3O, can be reproduced more accurately by chemical models if the gas-phase reaction OH + $CH_3OH \rightarrow CH_3O + H_2O$ is included using the measured rate at very low temperatures.[9, 16]

The formation of biomolecules such as amino acids from COMs under pre-biotic conditions has attracted much interest.[17] The amino acid glycine (NH_2CH_2COOH), a building block for proteins which are essential components of all living systems, has been observed in the coma of a comet.[18] The peptide bond (NH-C=O) plays a key role in linking of amino acids into peptide chains and proteins, it contains all the components necessary for the formation of

nucleic polymers under prebiotic conditions.[1] However, only two molecules containing this bond have been observed in space, formamide, NH_2CHO[2] and acetamide, $NH_2C(O)CH_3$.[3]

In a previous paper[19] we studied the low-temperature kinetics of the gas-phase neutral-neutral reaction of the amidogen radical, NH_2, and formaldehyde (CH_2O, ubiquitously found in space), $NH_2 + CH_2O \rightarrow NH_2CHO + H$, which had been suggested in theoretical studies as a viable route to form the simplest carboxylic acid amide, formamide, NH_2CHO.[20-22] There are two main exothermic product channels for this reaction; a hydrogen-abstraction channel in which the NH_2 abstracts an H atom from formaldehyde to produce ammonia, NH_3, and the formyl radical, CHO, and an addition-elimination channel in which the NH_2 first attacks the C of the formaldehyde to form a bound adduct, which then goes on to eliminate an H atom and produce formamide. Previous theoretical calculations of this reaction reached different conclusions. One study,[21] in which the authors argue for omitting the barrier to adduct formation, predicts the reaction leading to formamide formation to have an inverse temperature dependence, with the rate coefficient becoming large at $\sim 3 \times 10^{-10}$ cm^3 molecule^{-1} s^{-1} at 10 K. Another theoretical study[23] found that when zero-point energy was included there was a significant barrier to adduct formation and the $NH_2 + CH_2O$ reaction does not play a significant role in formation of formamide. Using a pulsed Laval nozzle apparatus equipped with laser-flash photolysis and laser-induced fluorescence spectroscopy we made the first experimental study of the low-temperature rate coefficient for this reaction.[19] No loss of NH_2 could be observed via reaction with CH_2O, and we placed an upper limit on the rate coefficient of $<6 \times 10^{-12}$ cm^3 molecule^{-1} s^{-1} at 34 K. We combined ab initio calculations of the potential energy surface with Rice–Rampsberger–Kassel–Marcus (RRKM) calculations to predict a rate coefficient of 6.2×10^{-14} cm^3 molecule^{-1} s^{-1} at 35 K, consistent with the experimental results. The presence of a significant barrier, 18 kJ mol^{-1}, for the formation of formamide as a product, a channel for which tunnelling is not possible, means that only the H-abstraction channel producing $NH_3 + CHO$, in which the transfer of an H atom can occur by quantum mechanical tunnelling through a 23 kJ mol^{-1} barrier, is open at low temperatures.[19] The calculated rate coefficients were used in an astrochemical model, which demonstrated that this reaction produces only negligible amounts of gas-phase formamide under interstellar and circumstellar conditions. We concluded therefore that the gas-phase reaction of NH_2 with CH_2O is not an important source of formamide at low temperatures in interstellar environments.[19]

In this paper we have performed an experimental and theoretical study of the kinetics of the reaction of NH_2 with acetaldehyde, the next aldehyde in the homologous series after formaldehyde, for which there are three energetically favourable channels (ΔH calculated in this study, see Section 4):

		$\Delta H^\circ_{(0\,K)}$ (kJ mol^{-1})	
$NH_2 + CH_3CHO$	$\rightarrow NH_3 + CH_3CO$	- 72	(R1a)
	$\rightarrow NH_3 + CH_3CHO$	- 43	(R1b)
	$\rightarrow NH_2COCH_3 + H$	- 30	(R1c)

Reaction R1 therefore is both a potential source of gas-phase organic radicals (CH_3CO and CH_2CHO *via* reactions R1a and R1b respectively), and of acetamide (NH_2COCH_3, *via* reaction R1c), the largest interstellar molecule with a peptide bond that has so far been observed in space. Acetamide was first detected in the interstellar medium in 2006 by Hollis, *et al.*[3] in both absorption and emission at radio frequencies toward the star-forming region Sagittarius B2(N)

with the 100 m Green Bank Telescope, within a cold halo region at ~ 8 K. Hollis, *et al.*[3] suggested that the exothermic but spin-forbidden gas-phase radiative-association reaction $NH_2CHO + CH_2 \rightarrow CH_3CONH_2 + h\nu$ may account for acetamide formation in this region, but stated that as there may be an activation barrier (likely > 10 kJ mol^{-1}), a transient thermal shock known to be prevalent in this star-forming region, was needed to overcome the barrier. Further observations of acetamide towards Sgr B2(N) were made by Halfen, *et al.*[24], who hypothesised that the similarity in the abundances and spatial distribution of formamide and acetamide in this region suggested a synthetic connection between the two species. The abundance of acetamide was similar to that of acetaldehyde, so was one of the most abundant COMs in Sgr B2(N). Acetamide was first observed on a comet via mass spectrometry following the touchdown in 2014 of the Philae lander on comet 67P/Churyumov–Gerasimenko.[18, 25-26] Acetamide could also be formed on ice mantles of interstellar grains, for example by the addition of CH_3 to HNCO with subsequent hydrogenation;[24] however, in cold clouds at around 10 K desorption of the refractory acetamide into the gas-phase seems unlikely.

Although some ion-molecule reactions, electron-molecule recombinations and neutral-neutral reactions have been suggested for interstellar acetamide formation,[24, 27] the low temperature behaviour of the neutral-neutral gas-phase reaction NH_2+CH_3CHO as a source is unexplored, with only one kinetics study performed for this reaction at higher temperatures between 297 – 543 K. Ths study[28] reported an Arrhenius-type behaviour for the rate coefficient, with a best-fit to the data giving $k(T) = 3.48 \times 10^{-13} \exp[(-10400 \pm 200)/RT]$ cm^3 $molecule^{-1}$ s^{-1}, with $k(298\ K) = 5.18 \times 10^{-15}$ cm^3 $molecule^{-1}$ s^{-1} and an activation energy for H-atom abstraction of 10.4 kJ mol^{-1}.

Methodology

S2. Additional Details on the Experimental Setup

The use of a Laval nozzle expansion coupled with a PLP-LIF technique has been employed by this group to study a range of low temperature neutral-neutral reactions, including reactions of OH with unsaturated hydrocarbons[29] and VOCs,[8, 11, 15, 30] $^1CH_2$ (singlet methylene) with atmospheric gases and hydrocarbons,[31-32] CH with CH_2O,[33] and NH_2 with CH_2O.[19] In the current study, we employ the same technique to study the low temperature reaction of NH_2 with CH_3CHO. As the experimental apparatus employed in the current and previous studies has been discussed in detail elsewhere,[8, 11, 29-30] only a brief overview is given here.

The low temperatures employed in this study were obtained by the isentropic expansion of a gas mixture from a high pressure reservoir to a low pressure chamber through a Laval nozzle, producing a thermalized low temperature gas flow that is stable for several centimetres from the nozzle exit. The gas mixture is pulsed into the 1 cm^3 reservoir from a high-pressure ballast by two pulsed solenoid values (Parker 9 series), fired at a pulse repetition rate of either 5 or 10 Hz, with a pulse duration of around 10 ms. A set of 4 nozzles were used during the experiments to achieve flow temperatures of between 29 and 107 K. The density and temperature profile of the flows were characterized by impact pressure measurements, and the temperature of several of the uniform flows confirmed by rotationally resolved LIF spectroscopy.[31, 33]

The gas mixture introduced to the reservoir consists primarily of an inert bath gas (Ar (99.9995 %, BOC), He (99.9995 %, BOC), or N_2 (99.9995 % , BOC)), together with smaller amounts of the NH_2 precursor (NH_3 (99.98 %, BOC)), the CH_3CHO co-reagent (Sigma-Aldrich, ≥ 99.0 %), and CH_4 (99.995 %, BOC). These reagent and bath gases were combined in the required quantities in a mixing manifold using calibrated mass flow controllers (MFCs; MKS Instruments). Both the bath gases and the CH_4 were introduced as pure gases, while the NH_3 was introduced as a dilute mixture of ~ 10 % in Ar. The dilute NH_3 flow typically accounted for less than 0.2 % of the total flow, resulting in ~ 0.02 % NH_3 present in the gas expansions. The CH_3CHO co-reagent was introduced by entraining CH_3CHO vapour in a flow of the bath gas passing through a glass bubbler (a modified Dreschel bottle) containing CH_3CHO liquid. The bubbler, which was maintained at 0 °C using an ice bath, was located before the relevant mass flow controller. By measuring the pressure of the bath gas over the CH_3CHO, the concentration of CH_3CHO entrained in the gas flow was determined *via* its known vapour pressure at 0 °C.[34] In practice, the vapour pressure of the CH_3CHO in the bubbler, as measured by a pressure gauge (Druck DPI 104), was shown to reduce over time, suggesting the slow formation of larger oxygenated and low volatility hydrocarbons from the CH_3CHO. Thus, the vapour pressure of the CH_3CHO as measured each day was used to calculate the CH_3CHO concentration entrained in the gas flow, and the CH_3CHO replaced regularly. This concentration of CH_3CHO in the flow was confirmed by UV absorption spectroscopy, carried out using 253.7 nm light from a Hg Pen-ray lamp, a 1 m length absorption cell, and a PMT (Hamamasu type H9306-13) fitted with a monochromator set at 253.7 nm (Minichrom, 300 μm slits) and connected to a digital oscilloscope (LeCroy LT262). The absorption cell was located after the mixing manifold and prior to the gas ballast, and the CH_3CHO concentrations determined using an absorption cross section of 1.6×10^{-20} cm^2

molecule^{-1} as taken from the MPI-Mainz Spectral Atlas.[35] The calculated and measured CH_3CHO concentrations were typically within 20 % of each other.

In previous studies, the reagent and precursor gases were mixed with the bath gas in a mixing manifold before entering the gas ballast. However, it was found that when gas flows containing NH_3 with formaldehyde co-reagent were mixed,[19] a misty film would form on the windows of the absorption cell, causing inaccuracies in the absorption spectroscopy measurements. This film was attributed to the formation of a salt from the reaction of the basic NH_3 with the slightly acidic formaldehyde, and as such the NH_3 precursor flow was redirected so that it only mixed with the other gas flows just before entering the gas ballast, after the other gases had passed through the absorption cell. As we would expect the same issue to arise between NH_3 and CH_3CHO, the same flow setup was adopted in these experiments. Indeed, in our experiments we do observe a decrease in the NH_2 LIF signal with increasing CH_3CHO concentrations (which is not the result of quenching of the NH_2 fluorescence signal by CH_3CHO, as the NH_2 fluorescence lifetime does not appear to change significantly as we add CH_3CHO), suggesting some reaction between NH_3 and CH_3CHO is occurring either in the ballast tank and/or the low temperature expansion. Despite this we still observed satisfactory NH_2 LIF signal even at high CH_3CHO concentrations, indicating that sufficient NH_3 remained in the gas-flow to be photolyzed. No corrections to the CH_3CHO concentrations were made to account for this reaction, as the CH_3CHO concentrations used in our experiments were typically far in excess of the NH_3 concentrations.

NH_2 radicals were generated from the PLP of NH_3 at 213 nm (Reaction R2) by the 5th harmonic of a Nd:YAG laser (Quantel Q-Smart 850), with a typical pulse energy of ~10 mJ. The photolysis laser was introduced co-linearly with the axis of the expanded gas flow, to produce a uniform radical density. NH_2 radicals were observed by time-resolved LIF spectroscopy, probing the $A\ ^2A_1$ (0,9,0) ← $X\ ^2B_1$ (0,0,0) transition near 597.7 nm[36-37] using the output of Nd:YAG pumped dye laser (a Quantel Q-smart 850 pumping a Sirah Cobra-Stretch). The probe laser was introduced perpendicularly to the photolysis laser beam, crossing the gas flow at the furthest distance from the exit of the nozzle before the flow broke up due to turbulence (typically between 8 and 30 cm depending on the nozzle and bath gas). The non-resonant fluorescence at ~ 620 nm was collected *via* a series of lenses through an optical filter (Semrock Brightline interference filter, λ_{max} = 620 nm, fwhm = 14 nm), and observed by a temporally gated channel photomultiplier (CPM; PerkinElmer C1952P), mounted at 90° to both laser beams. The signal from the CPM was recorded using a digital oscilloscope (LeCroy Waverunner LT264), whose output was sent to a computer using a custom LabView program. The temporal evolution of the LIF signal was recorded by varying the time delay between the photolysis and probe lasers. A typical time-resolved LIF profile (Figure 1) consisted of 165 delay steps and resulted from the average or between 5 and 15 individual delay scans.

$$NH_3 + h\nu\ (213\ nm) \rightarrow NH_2 + H \qquad (R1)$$

Photolysis of NH_3 produces both ground and vibrationally excited NH_2,[37-38] and as a consequence of this the profiles of NH_2 (v = 0) exhibit a growth resulting from the relaxation of vibrationally excited NH_2 (see Figure 1). As has been discussed previously,[19] this poses a problem for conducting kinetics measurements of NH_2 in our system, as the timescale for kinetic experiments is restricted by the length of the uniform supersonic flow, with dynamic times in our system ranging from ~ 100 to 500 μs depending on the nozzle and bath gas used.

By adding up to 3 % CH_4, which has been shown to efficiently relax vibrationally excited NH_2 whilst not changing the conditions of the uniform expansion, to our low temperature flows, we were able to increase the initial growth rate of the NH_2 (v = 0) signal, thus increasing the effective timescale in which we can monitor the loss the NH_2 (v = 0) signal.

Experiments looking at the dimerization of CH_3CHO at low temperatures were conducted using the same experimental apparatus as described above. CH_3CHO has a broad absorption feature between ~ 230 and 345 nm.[39] CH_3CHO was observed by probing the $^3(n,\pi^*)$ $A\ ^3A'' \leftarrow X\ ^1A'$ transition within this feature at 308.0 nm, using the frequency doubled output of a Nd:YAG pumped dye laser (same system as described above with a BBO doubling crystal). The non-resonant fluorescence at $\lambda > 390$ nm was discriminated using a long pass Perspex filter.

Some additional experiments were also carried out observing the production of OH radicals from the reaction of CH_3CO with O_2 (R4), in order to obtain the yield of CH_3CO produced from reaction R1 (*via* channel R1a). As a part of these experiments, the temporal removal of OH by CH_3CHO, both with and without O_2 present, was also recorded, with the OH produced by the PLP of tert-butyl hydrogen peroxide ($(CH_3)_3COOH$; tBuOOH). These experiments were all conducted using the same experimental apparatus as described above. The tBuOOH precursor was introduced in the same method as the CH_3CHO co-regent, by entraining its vapour in a flow of bath gas passing through a bubbler containing tBuOOH liquid (Alfa-Aesar, 90 % aqueous solution). The concentration of tBuOOH in our low temperature flows was estimated using its known vapour pressure at room temperature, and typically accounted for < 0.1 % of the total flow. These concentrations of tBuOOH were too low to measure directly by absorption spectroscopy, however by carrying out absorbance measurements at higher flows of tBuOOH we were able to produce a calibration plot of the tBuOOH concentration *vs* MFC flow rate, and use the flow rate to determine tBuOOH concentrations when they were too low for absorbance measurements. An absorption cross section of 1.5×10^{-20} cm^2 molecule^{-1} for tBuOOH at 253.7 nm, as taken from the MPI-Mainz Spectral Atlas,[35] was used for these measurements. OH radicals were observed by probing the $A\ ^2\Sigma^+$ (v' =0) $\leftarrow X\ ^2\Pi$ (v'' = 0) transition at ~ 307.9 nm, using the laser system as described above. The resonant fluorescence was collected using a gated PMT, in which the scattered laser probe light was gated out, and fitted with an interference filter centred at 308.5 nm (Barr Associates, fwhm = 5nm).

Experimental Rate Coefficients for the reaction NH_2+ CH_3CHO

Figure S3. Temperature dependent rate coefficients for the reaction between NH_2 + CH_3CHO (R1). As we are unable to simply dial up temperatures and pressures in our experiments, we are unable to vary the temperature while keeping the pressure constant. Instead, to demonstrate the temperature dependence, we have grouped together data collected at the same approximate density and collected in the same bath gas. See Table 1 in the main text for full set of temperatures and pressures employed.

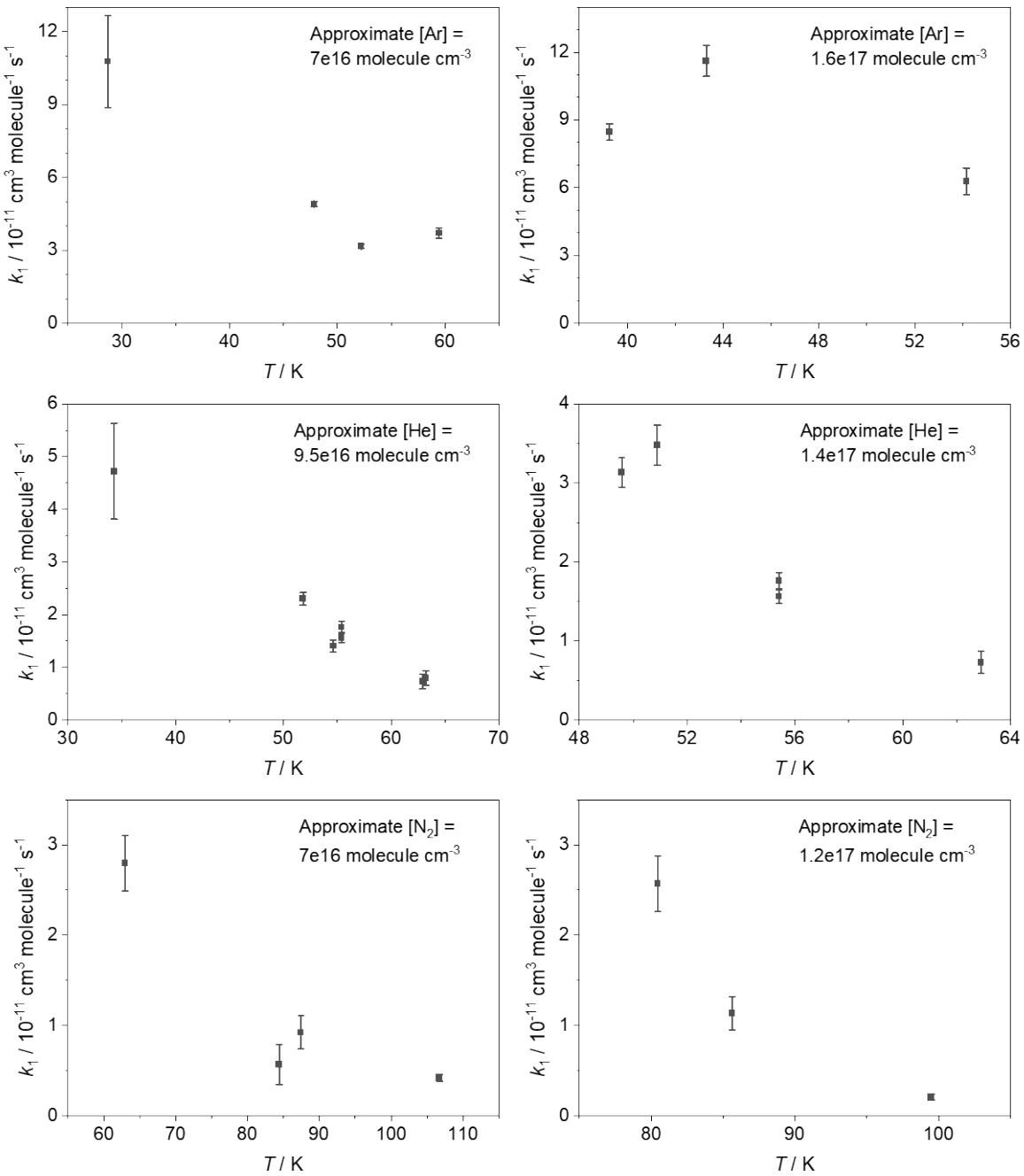

Figure S4. Pressure dependent rate coefficients for the reaction between NH_2 + CH_3CHO (R1), collected in Ar (top panel), He (middle panel), and N_2 (bottom panel). The approximate temperatures (as it is slightly different for each pressure, see Table x) the measurements were made at are shown in the legends.

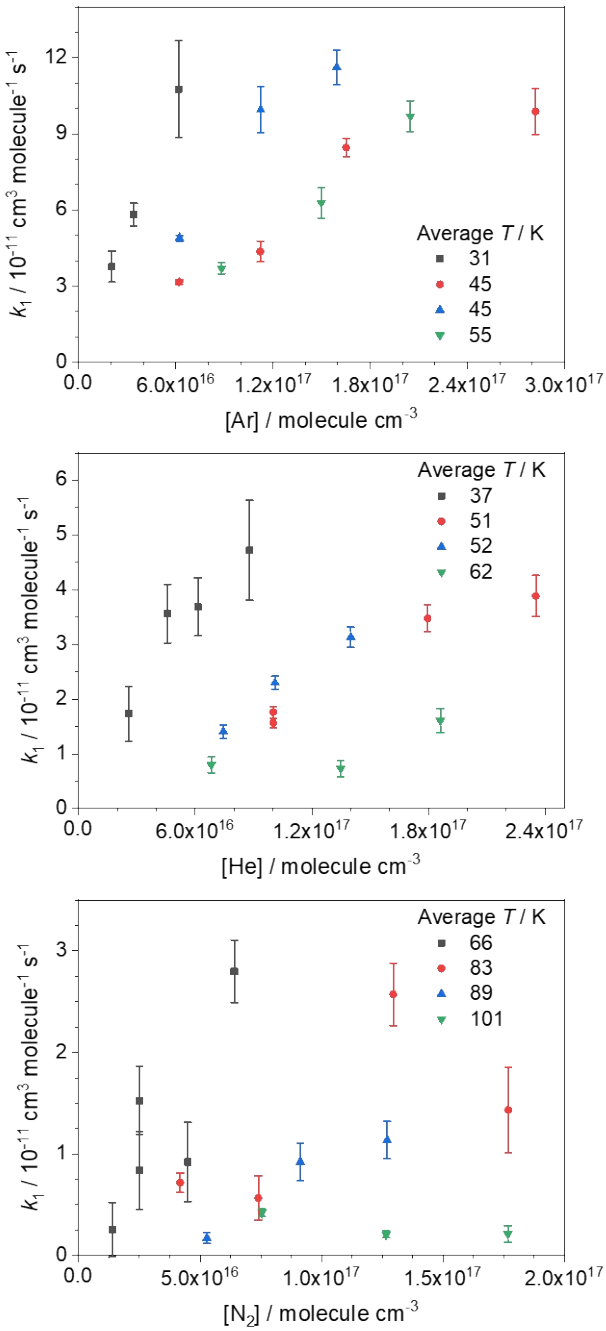

Determination of Experimental OH / CH_3CO Yields

Figure S5. OH traces collected at 67.1 K, a total N_2 density of 2.5×10^{16} molecule cm^{-3}, and $[CH_3CHO]$ of 1.9, 3.0 and 5.3×10^{13} molecule cm^{-3} (black squares, red triangles, and blue circles respectively). Solid lines are the least squares fitting of a single exponential fit to the traces from which k'_{obs} is obtained:

$$[OH]_t = [OH]_0 . exp^{(-k'_{obs} \cdot t)}$$

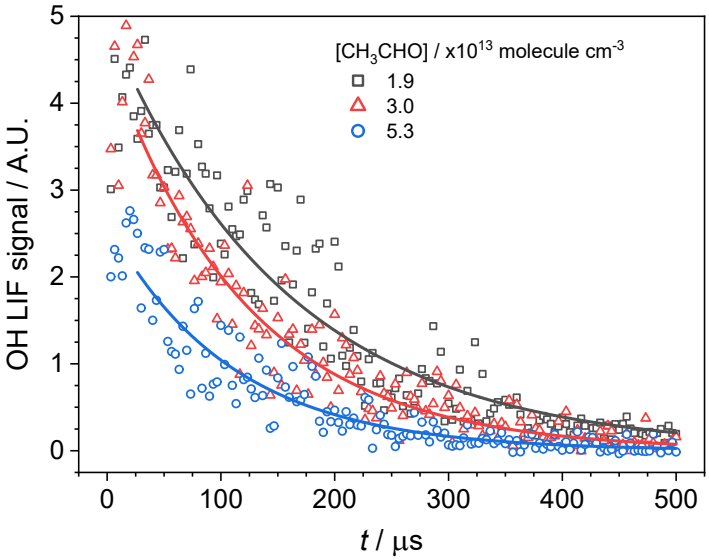

S6. Further details on CH_3CO yield determinations

To address the first issue in determining the yield for CH_3CO production from R1, that is understanding how many OH radicals have been produced relative to the initial number of NH_2 radicals produced, we used the following procedure. Note, the figures and tables presented in this section are not cited in the main text, but are given here for completeness.

1. The OH LIF signal is calibrated using a known concentration of tBuOOH (1.06×10^{12} molecule cm^{-3}), and its absorption cross-section at 213 nm ($\sigma = 8.5 \times 10^{-20}$ cm^2 $molecule^{-1}$).[35]

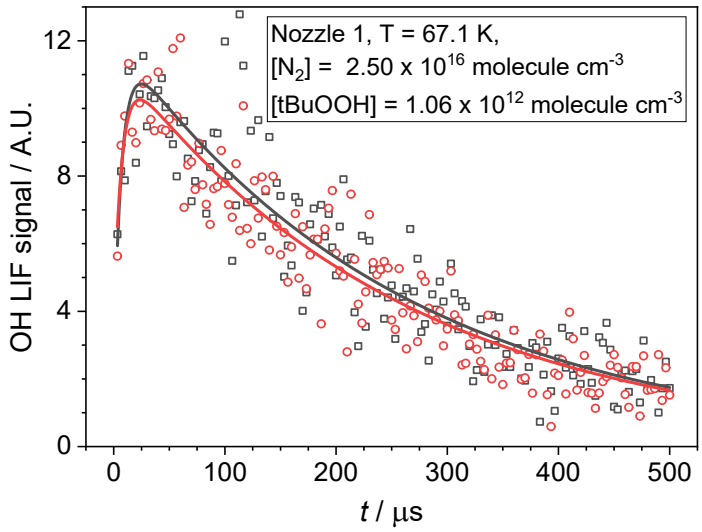

f_{OH}, the observed OH fluorescence signal, is extracted from a bi-exponential fit to the OH LIF signal. From the above figure, using the equation below, we extract an f_{OH} = 11.6 A.U. Black and red traces are repeats of the same experiment.

$$[OH]_t = f_{OH}\left(\frac{k'_{growth}}{k'_{loss} - k'_{growth}}\right)[OH^*]_0\left(e^{-k'_{growth}.t} - e^{-k'_{loss}.t}\right) + [OH]_0.e^{-k'_{loss}.t}$$

Product of [tBuOOH] × σ(tBuOOH) = n.σ tBuOOH = 8.99×10^{-8} cm^{-1}.

2. Get f_{OH} from the OH yield experiments in which NH_3 is photolysed in the presence of CH_3CHO and O_2, again from a bi-exponential fit to the data. Same conditions as above (Nozzle 1, T = 67.1 K, $[N_2] = 2.50 \times 10^{16}$ molecule cm^{-3}, same photolysis energy and PMT settings).

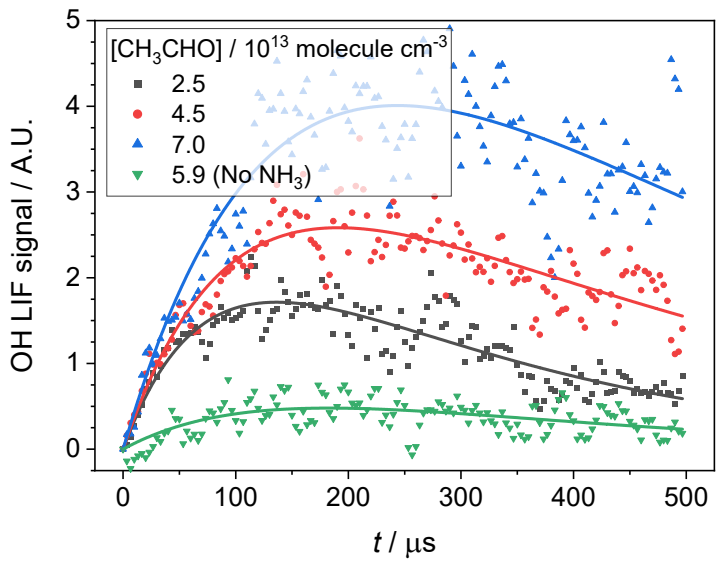

We can compare these f_{OH} values to that from tBuOOH and calculate an effective [tBuOOH] that would give this signal, and calculate effective n.σ tBuOOH.

$[CH_3CHO]$ / × 10^{13} molecule cm^{-3}	f_{OH}	Ratio f_{OH} from NH_2 : f_{OH} from tBuOOH	Effective [tBuOOH] / × 10^{11} molecule cm^{-3}	n.σ tBuOOH / × 10^{-8} cm^{-1}
2.50	2.98	0.26	2.72	2.31
4.50	4.30	0.37	3.92	3.33
7.00	8.34	0.72	7.60	6.46

3. Determine how much NH_2 relates to each of these OH signals. This can be estimated from the concentration of NH_3 in our experiments and its absorbance cross-section at 213 nm ($\sigma = 2.0 \times 10^{-18}$ cm^2 $molecule^{-1}$).[35] These experiments were carried out with $[NH_3] = 9.5 \times 10^{12}$ molecule cm^{-3}. However, from experiments observing NH_2 removal with CH_3CHO, we see the NH_2 LIF signal, f_{NH2}, decreasing with increasing CH_3CHO, suggesting some of the NH_3 is lost to reaction with CH_3CHO prior to the expansion through the Laval nozzle. The reduction in NH_3 with CH_3CHO can be determined by looking at the reduction in the NH_2 signal with CH_3CHO compared to the NH_2 signal with no CH_3CHO (again for experiments conducted under the same conditions, Nozzle 1, T = 67.1 K, $[N_2] = 2.50 \times 10^{16}$ molecule cm^{-3}, same photolysis energy). This was done by fitting a single exponential loss to the f_{NH2} values and using this fit to determine the reduction in f_{NH2} with CH_3CHO.

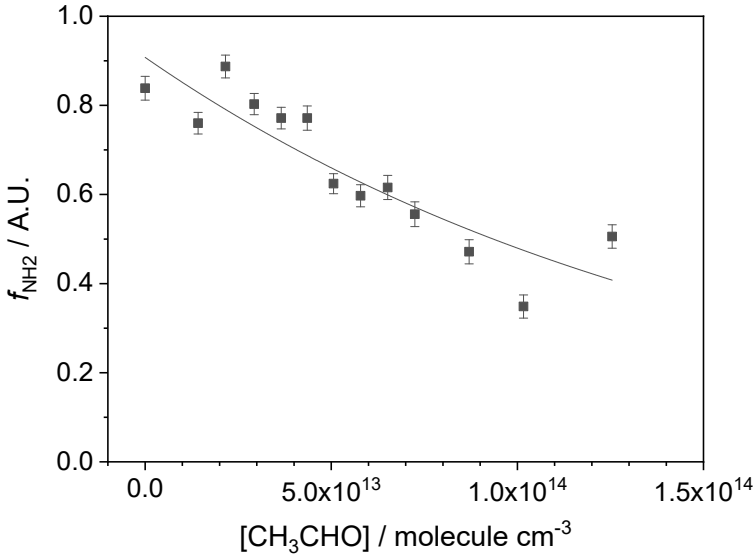

4. With both the concentration and absorption cross section of NH_3 we can calculate the n.σ product. Finally, comparing the n.σ products for tBuOOH and NH_3 we can determine the ratio of NH_2 radials that were converted into OH radicals.

[CH_3CHO] / × 10^{13} molecule cm^{-3}	Ratio NH_2 signal with CH_3CHO to without CH_3CHO	[NH_3] / × 10^{12} molecule cm^{-3}	n.σ NH_3 / × 10^{-5} cm^{-1}	Ratio NH_2 : OH
2.50	0.85	8.10	1.62	701:1
4.50	0.75	7.13	1.43	428:1
7.00	0.64	6.08	1.22	188:1

5. Determine how much NH_2 in each experiment is actually removed by CH_3CHO, rather than from diffusional losses. This can be determined from experiments observing the loss of NH_2 with CH_3CHO, again conducted under the same conditions (T = 67.1 K, [N_2] = 2.50 × 10^{16} molecule cm^{-3}) from which we obtain a rate coefficient of k_1 = 1.19 × 10^{-11} cm^3 molecule^{-1} s^{-1}. Using this we can correct the product of n.σ for NH_3, and finally determine the ratio of NH_2 radicals that are removed by CH_3CHO that were converted in OH radicals.

[CH_3CHO] / × 10^{13} molecule cm^{-3}	k' diffusion / s^{-1}	k' CH_3CHO / s^{-1}	% NH_2 removal with CH_3CHO	Corrected n.σ NH_3 / × 10^{-7} cm^{-1}	Ratio NH_2 : OH
2.50	4600	296	6.1	9.8	42:1
4.50	4600	533	10.4	14.8	44:1
7.00	4600	830	15.3	18.6	29:1

As can be seen from the above table, there is reasonable agreement in the amount of OH converted per NH_2 radical (the final column which is the ratio NH_2:OH) even as the concentration of CH_3CHO is varied. Taking an average of these three values, we

determine that for every NH_2 radical that is removed by a CH_3CHO molecule, only 0.027 OH radicals are produced. There is one further correction to make to this number when determining the CH_3CO yield from R1 (i.e. the branching ratio for reaction R1a), and that is to account for the non-unity conversion of CH_3CO with O_2 to OH. We determined an OH yield from $CH_3CO + O_2$ of 0.94 (see main text, Section 3.3). Accounting for this, we determine a CH_3CO yield from R1 of 0.029. The most significant error in this calculation is in the rate coefficient for $NH_2 + CH_3CHO$, which has an error of almost 50 %. As we expect the other errors to be significantly smaller than this (such as the errors in the absorbance cross-sections and in the determination of the tBuOOH concentration), we assign the CH_3CO yield from R1 at T = 67.1 K and $[N_2] = 2.50 \times 10^{16}$ molecule cm^{-3} as 0.029 ± 0.014.

Using the same procedure we have determined the yield of CH_3CO from the experiments carried out in He, at T = 35.0 K.

1. The OH LIF signal is calibrated using a known concentration of tBuOOH (1.06×10^{12} molecule cm^{-3}), and its absorption cross-section at 213 nm ($\sigma = 8.5 \times 10^{-20}$ cm^2 $molecule^{-1}$).[35]

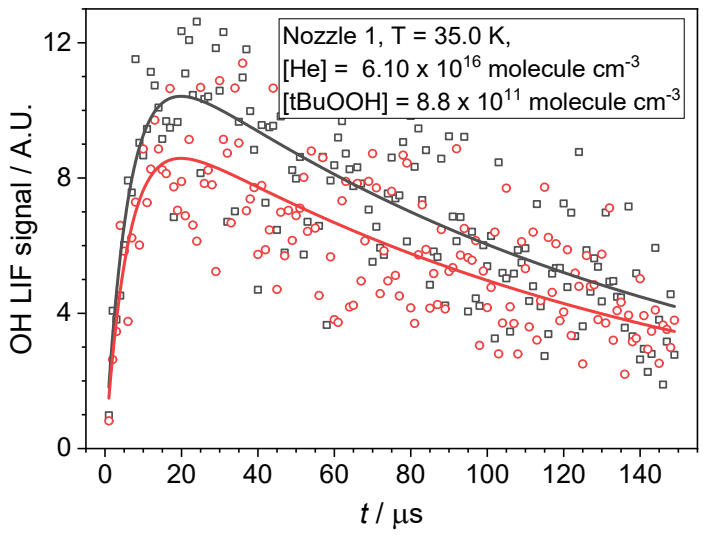

f_{OH}, the observed OH fluorescence signal, is extracted from a bi-exponential fit to the OH LIF signal. From the above figure, using the equation below, we extract an f_{OH} = 11.0 A.U. Black and red traces are repeats of the same experiment.

$$[OH]_t = f_{OH}\left(\frac{k'_{growth}}{k'_{loss} - k'_{growth}}\right)[OH^*]_0\left(e^{-k'_{growth}.t} - e^{-k'_{loss}.t}\right) + [OH]_0.e^{-k'_{loss}.t}$$

Product of [tBuOOH] × σ(tBuOOH) = n.σ tBuOOH = 7.50×10^{-8} cm^{-1}.

2. Get f_{OH} from the OH yield experiments in which NH_3 is photolysed in the presence of CH_3CHO and O_2, again from a bi-exponential fit to the data. Same conditions as above

(Nozzle 1, T = 35.0 K, [He] = 6.13 × 10^{16} molecule cm^{-3}, same photolysis energy and PMT settings).

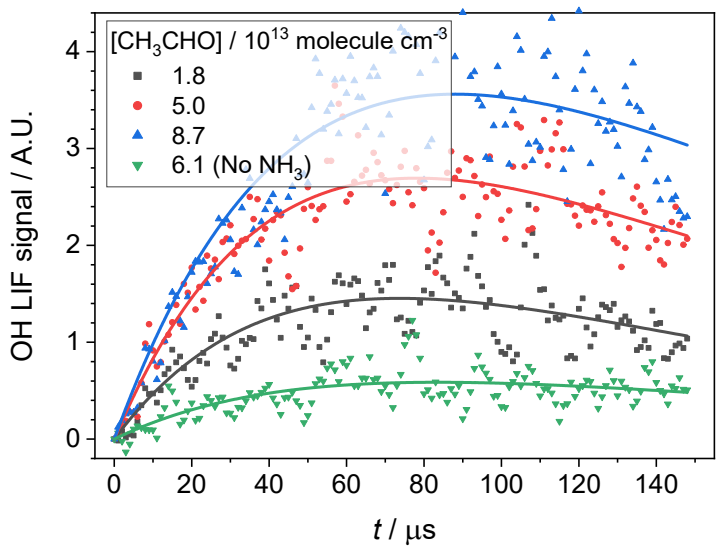

Can compare these f_{OH} values to that from tBuOOH and calculate an effective [tBuOOH] that would give this signal, and calculate effective n.σ tBuOOH.

$[CH_3CHO]$ / × 10^{13} molecule cm^{-3}	f_{OH}	Ratio f_{OH} from NH_2 : f_{OH} from tBuOOH	Effective [tBuOOH] / × 10^{11} molecule cm^{-3}	n.σ tBuOOH / × 10^{-8} cm^{-1}
1.80	3.88	0.35	3.11	2.65
5.00	6.00	0.55	4.82	4.09
8.70	8.36	0.76	6.71	5.70

3. Determine how much NH_2 relates to each of these OH signals. This can be estimated from the concentration of NH_3 in our experiments its absorbance cross-section at 213 nm (σ = 2.0 × 10^{-18} cm^2 $molecule^{-1}$).[35] These experiments were carried out with $[NH_3]$ = 8.0 × 10^{12} molecule cm^{-3}. Again we account for the reduction in NH_3 by CH_3CHO by looking at the reduction in the NH_2 signal with CH_3CHO as compared to the NH_2 signal with no CH_3CHO (for experiments conducted under the same conditions, Nozzle 1, T = 35.0 K, [He] = 6.13 × 10^{16} molecule cm^{-3}, same photolysis energy). This was done by fitting a single exponential loss to the f_{NH2} values, and using this fit to determine the reduction in f_{NH2} with CH_3CHO.

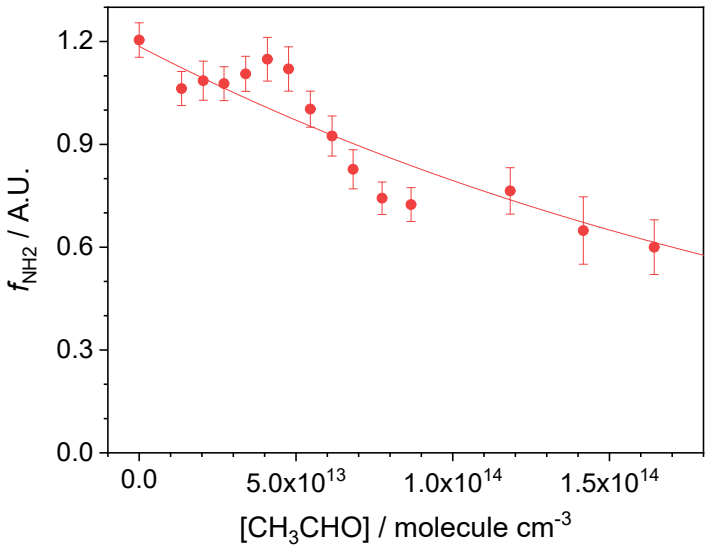

4. With both the concentration and absorption cross section of NH_3 we can calculate the n.σ product. Finally, comparing the n.σ products for tBuOOH and NH_3 we can determine the ratio of NH_2 radials that were converted in OH radicals.

[CH_3CHO] / × 10^{13} molecule cm^{-3}	Ratio NH_2 signal with CH_3CHO to without CH_3CHO	[NH_3] / × 10^{12} molecule cm^{-3}	n.σ NH_3 / × 10^{-5} cm^{-1}	Ratio NH_2 : OH
1.80	0.93	7.44	1.49	562:1
5.00	0.82	6.55	1.31	320:1
8.70	0.71	5.65	1.13	198:1

5. Determine how much NH_2 in each experiment is actually removed by CH_3CHO, rather than from diffusional losses. This can be determined from experiments observing the loss of NH_2 with CH_3CHO, again conducted under the same conditions (T = 35.0 K, [He] = 6.13 × 10^{16} molecule cm^{-3}) from which we obtain a rate coefficient of k_1 = 3.69 × 10^{-11} cm^3 molecule^{-1} s^{-1}. Using this we can correct the product of n.σ for NH_3, and finally determine the ratio of NH_2 radicals that are removed by CH_3CHO that were converted in OH radicals.

[CH_3CHO] / × 10^{13} molecule cm^{-3}	k' diffusion / s^{-1}	k' CH_3CHO / s^{-1}	% NH_2 removal with CH_3CHO	Corrected n.σ NH_3 / × 10^{-7} cm^{-1}	Ratio NH_2 : OH
2.50	10500	664	5.9	8.9	33:1
4.50	10500	1845	14.9	19.6	48:1
7.00	10500	3210	23.4	26.4	46:1

As can be seen from the above table, there is reasonable agreement in the amount of OH converted per NH_2 radical (the final column which is the ratio NH_2:OH) even as the concentration of CH_3CHO is varied. Taking an average of these three values, we

determine that for every NH_2 radical that is removed by a CH_3CHO molecule, only 0.024 OH radicals are produced. Accounting for the non-unity conversion of CH_3CO with O_2 to OH, we determine a CH_3CO yield from R1 of 0.026. The error in the rate coefficient for NH_2 + CH_3CHO at this temperature is significantly smaller than for the N_2 case at 67.1 K, being only around 15 % (compared to almost 50 % for the N_2 case). Errors in the absorbance cross sections used in this calculation, and in the determination of tBuOOH concentration are likely around 10 %. As such we assign the CH_3CO yield from R1 at T = 35.0 K and [He] = 6.14×10^{16} molecule cm^{-3} as 0.026 ± 0.008.

Ab initio calculations of the NH_2 + CH_3CHO potential energy surface

Figure S7. Optimised structures of the stationary points on the potential energy surface for NH_2 + CH_3CHO, calculated at the M062X/aug-cc-pVTZ level of theory.

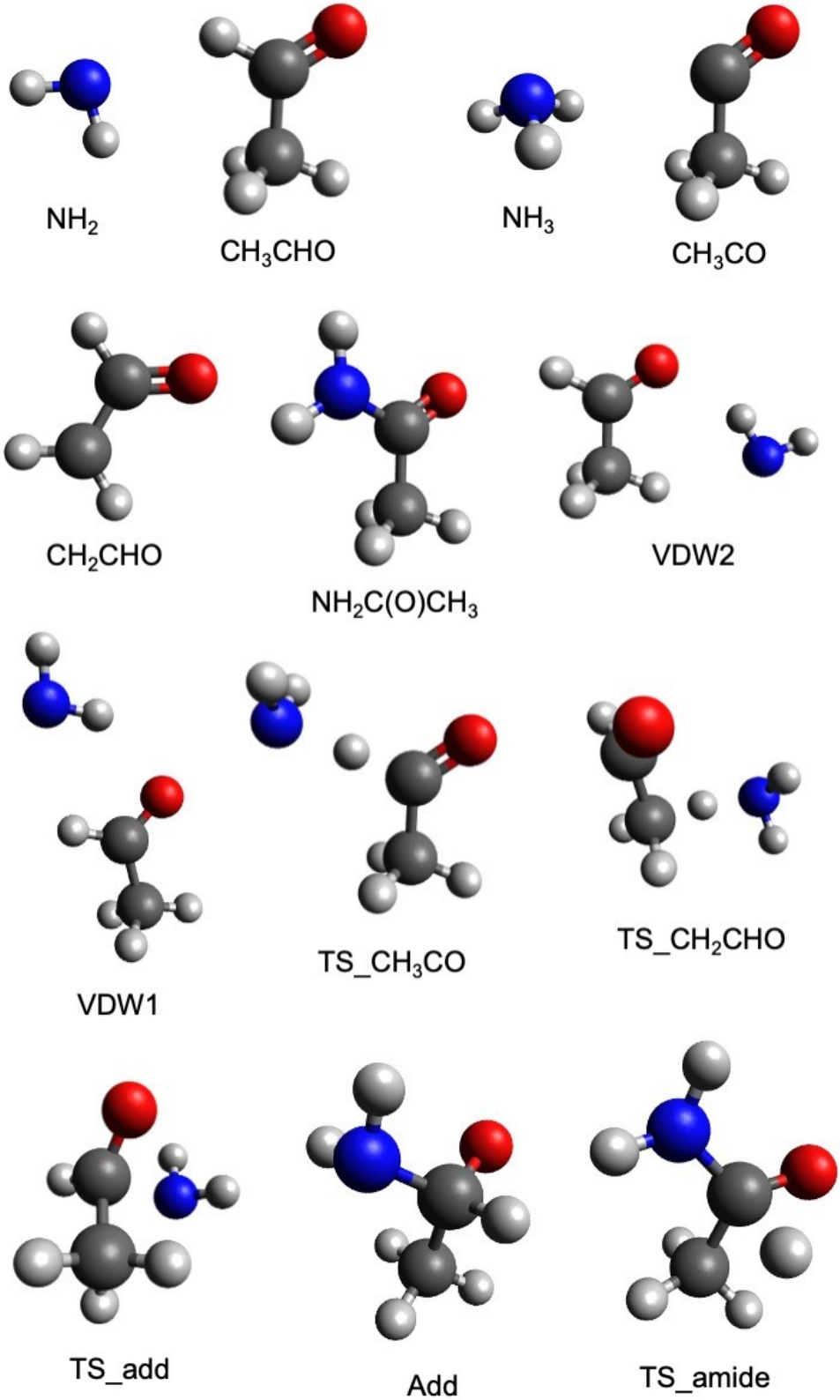

Table S8. Optimized geometries of the stationary points on the potential energy surface for NH_2 + CH_3CHO shown in Figure 7, calculated at the M062X/aug-cc-pVTZ level of theory.

Molecule	Atom, (x, y, z) cartesian coordinates / Å			
NH_2	N	-0.32996800	-0.74279100	0.02683100
	H	0.03622300	-1.69829700	-0.01951600
	H	0.03623600	-0.30520600	-0.82381200
CH_3CHO	C	-0.38354600	0.55805300	0.00919700
	H	0.27434600	-0.29351400	-0.17297800
	H	-0.39390600	1.21803100	-0.85356500
	H	-1.38166800	0.15521600	0.18998100
	C	0.08280500	1.29322600	1.22909700
	H	0.12602700	0.69534800	2.15979200
	O	0.39818600	2.45080400	1.24355300
NH_3	N	-0.04248000	0.12703500	0.00000200
	H	0.33209300	-0.81320500	-0.00000100
	H	0.33210500	0.59712000	0.81427900
	H	0.33209300	0.59712000	-0.81428000
CH_3CO	C	-1.13580300	0.24273400	-0.03370800
	H	-0.80890700	-0.77617300	0.17490600
	H	-0.75153600	0.51553400	-1.01679800
	H	-2.22561000	0.31010700	-0.01314000
	C	-0.52164800	1.15743300	0.98734700
	O	-1.04697700	1.88044200	1.74592900
CH_2CHO	C	-1.89060400	0.70618900	0.03088800
	H	-1.89387000	1.31134800	-0.86350600
	H	-2.31185700	-0.28748200	0.00961400
	C	-1.32467300	1.24089300	1.22566200
	H	-1.33843900	0.59529300	2.11771200
	O	-0.83922300	2.36252300	1.28470600
$NH_2C(O)CH_3$	C	1.41838600	0.81428300	-1.04838300
	H	1.66843500	-0.08890200	-0.49484200
	H	1.82153100	1.68567300	-0.54202200
	H	1.87126800	0.75126800	-2.03802900
	C	-0.07235000	0.99748400	-1.21388000
	O	-0.58894700	2.08841700	-1.31078200
	N	-0.79811800	-0.15357800	-1.27370500
	H	-0.37160000	-1.05831300	-1.20988500
	H	-1.78788300	-0.08566700	-1.43630600
VDW1	C	-0.41613300	0.67822400	0.10560600
	H	-0.48282500	-0.41065600	0.07253100
	H	0.23359700	0.97978200	-0.71785400
	H	-1.40138100	1.12119200	-0.00806600
	C	0.20636000	1.09378400	1.40127200
	H	1.21482300	0.69562700	1.61218100
	O	-0.32636400	1.82066300	2.20037300
	N	2.19704700	1.47886500	3.87363800
	H	2.46077800	1.86522500	4.78361600
	H	1.25893600	1.85745000	3.69777800

TS_CH_3CO	C	-0.11739000	0.67200100	0.38692600
	H	0.19495000	-0.35803800	0.56073300
	H	0.68105900	1.15351900	-0.17821300
	H	-1.05658800	0.70719800	-0.15900800
	C	-0.24616300	1.36201500	1.71312900
	H	0.80188400	1.33006700	2.33604000
	O	-1.21617100	1.88879100	2.15237100
	N	2.07080300	1.26995100	3.04615800
	H	1.69561000	0.88195500	3.91705000
	H	2.13684400	2.27269600	3.24589100
VDW2	C	-0.52218400	0.35513300	0.14572000
	H	-1.01590300	1.19734500	-0.34309400
	H	-1.28577200	-0.41030900	0.29749800
	H	0.28200600	-0.02807000	-0.47708600
	C	-0.01053000	0.80058500	1.47853600
	H	-0.76894500	1.20496600	2.17462400
	O	1.14069200	0.74603300	1.82498900
	N	2.77683500	-0.47848500	-0.54456800
	H	3.78645500	-0.64041100	-0.50217400
	H	2.54303800	-0.07101800	0.36823200
TS_CH_2CHO	C	-0.10764000	0.39719200	0.16087900
	H	1.04571200	0.01668300	-0.16813400
	H	-0.48761600	0.85240800	-0.74888200
	H	-0.64083000	-0.49407300	0.47447100
	C	0.16493200	1.33488700	1.26895700
	H	0.34951300	2.38639500	0.98475000
	O	0.23991700	0.99606700	2.42380200
	N	2.21837600	-0.64106900	-0.26452700
	H	1.88221800	-1.55288100	-0.58631700
	H	2.38773300	-0.78101800	0.73634600
TS_Add	C	-1.80603000	0.75863600	-0.04080000
	H	-1.52573700	-0.29139200	-0.01488600
	H	-1.53796400	1.17130500	-1.01511800
	H	-2.87977600	0.87060300	0.09638300
	C	-1.06541200	1.54118300	1.01027500
	H	0.00443400	1.30057800	1.10627700
	N	-1.56125400	0.54299600	2.64666400
	H	-1.10027500	1.08119100	3.38452900
	H	-2.55068500	0.79042300	2.73744900
	O	-1.49033300	2.61664500	1.44938200
Add	C	-1.81890300	0.75782800	0.04773300
	H	-1.56658700	-0.29900000	0.01401600
	H	-1.49383600	1.25149900	-0.86348500
	H	-2.89905200	0.86474300	0.14473000
	C	-1.13401200	1.37620000	1.27400800
	H	-0.04681800	1.29015800	1.14542500
	N	-1.50395200	0.65896200	2.47039400
	H	-1.08806300	1.09169400	3.28533600
	H	-2.50985500	0.67694000	2.59485400
	O	-1.45195500	2.71314500	1.24714500

TS_amide	C	-1.92047200	0.81043400	0.06117600
	H	-1.77713400	-0.26631000	0.13042300
	H	-1.41220300	1.19755200	-0.81615100
	H	-2.98777000	1.01907800	-0.02035700
	C	-1.40811200	1.53588500	1.29617200
	H	0.07874000	1.08467200	1.09404700
	N	-1.77076300	0.93796900	2.49622400
	H	-1.41522200	1.39321900	3.32225900
	H	-1.79815700	-0.06691200	2.53393900
	O	-1.10194000	2.73657900	1.26242300

Table S9. Relative energies of the stationary points on the potential energy surface for NH_2 + CH_3CHO shown in Figure 7. Electronic energies calculated at the CCSD(T)/aug-cc-pVTZ//M062X/aug-cc-pVTZ level of theory and zero-point energies at the M062X/aug-cc-pVTZ level of theory.

Molecule	Relative energy / kJ mol^{-1}
NH_2 + CH_3CHO	0
PRC1	–11.3
TS1	17.3
NH_3 + CH_3CO	–71.9
PRC2	–12.5
TS2	38.7
NH_3 + CH_2CHO	–43.4
TS3	22.4
Adduct	–28.6
TS4	23.4
CH_3CONH_2 + H	–30.1

Table S10. Rotational constants and unscaled vibrational frequencies of the stationary points on the potential energy surface for NH_2 + CH_3CHO shown in Figure 7, calculated at the M062X/aug-cc-pVTZ level of theory.

Molecule	Rotational constants / GHz	Wavenumber / cm^{-1}
NH_2	712.93038 387.58406 251.08298	1531.5886 3405.6604 3493.6840
CH_3CHO	57.34273 10.25604 9.19039	163.0217 513.5663 779.0266 900.9351 1138.1867 1146.0322 1381.6376 1430.3317 1466.0849 1475.7589 1865.7796 2944.0370 3061.8928 3124.6679 3177.7397
NH_3	299.87944 299.86305 189.07759	1031.9317 1659.0495 1659.6365 3508.5788 3633.1568 3634.3644
CH_3CO	84.85115 10.05365 9.51476	97.5784 468.9292 866.6931 955.3696 1049.5196 1353.0407 1459.2567 1461.8530 1985.8134 3062.1509 3158.2204 3161.5624
CH_2CHO	67.51344 11.54901 9.86199	455.4787 509.7045 758.0600 981.9680 990.3857 1169.9461 1409.2589 1481.2105 1629.1315 3004.7145 3176.0083 3290.8471

$NH_2C(O)CH_3$	10.92316	9.35601	5.20205	31.7408 192.0489 430.6848 523.1225 558.1449 656.4375 862.9309 989.8007 1059.5074 1124.8236 1349.0716 1410.1745 1475.4682 1494.4322 1619.8078 1815.1507 3079.2226 3148.1184 3185.2431 3620.2650 3761.8716
VDW1	20.28384	2.72350	2.43694	55.6568 99.1263 112.9618 154.8242 155.7337 285.3817 293.7395 521.7478 788.9190 907.1814 1141.2044 1155.9669 1382.0418 1447.6286 1464.8835 1473.8642 1540.5115 1846.6502 2987.4797 3063.3513 3125.4053 3180.0175 3389.7937 3486.8190
TS_CH_3CO	9.77287	4.13050	3.00151	–1200.8949 51.5501 82.6841 101.3744 209.8910 422.1135 612.8750 615.7110 800.4342 919.1571 932.2367 1131.7470 1249.9571 1367.7572 1397.0826 1460.4349 1464.5411 1535.3418 1909.5105 3068.4341 3139.6207 3176.9727 3407.0030 3495.5199
VDW2	10.27356	3.69276	2.76228	38.9721 66.4894 104.6598 145.9590 157.3993 286.0806 301.3625 527.0971 778.9759 905.1303 1149.6458 1151.9267 1386.6857 1434.5115 1467.6241 1480.0896 1540.7119 1852.8525 2954.3881 3058.4084 3120.6282 3174.8979 3390.0869 3486.7586
TS_CH_2CHO	13.03348	3.73154	3.17434	–1763.6131 48.7993 96.5360 162.8539 378.8652 511.9414 599.6075 676.8147 864.3537 928.8687 967.2125 1115.0167 1144.6584 1324.2884 1391.7473 1419.9615 1459.3245 1543.0341 1813.1255 2965.6825 3124.2843 3214.9062 3411.4196 3501.3848
TS_Add	9.82481	7.05492	4.71539	–441.3410 202.1770 209.0855 274.3182 392.1498 505.7420 683.0005 793.6056 885.7569 953.9560 1095.9959 1140.5138 1380.5501 1402.2874 1469.9607 1479.6699 1544.8232 1627.5916 2993.7140 3068.9930 3142.4992 3174.3743 3416.8154 3510.0638
Add	9.85698	8.53711	5.21715	215.2174 249.4492 362.2812 418.5156 495.8771 843.4580 874.0290 896.9706 984.9806 1036.7524 1151.8491 1243.0039 1249.3068 1383.8119 1392.1951 1484.9125 1495.6467 1655.0698 3007.3603 3079.0880 3158.6738 3181.6867 3523.4833 3609.1511
TS_amide	10.03827	8.77972	5.13009	–1138.4853 200.8816 387.5029 445.8028 496.0434 522.4663 593.1430 647.6512 695.5432 870.1973 988.1287 1062.8554 1138.5968 1316.7719 1395.3313 1474.4090 1486.0081 1610.6980 1652.7921 3075.2056 3148.5428 3186.5426 3589.4411 3712.3672

Figure S11. Fractional yield of the three product channels of the NH_2 + CH_3CHO reaction as a function of temperature at $P = 1 \times 10^{-16}$ molecule cm^{-3}, with Ar bath gas. Calculated using the full NH_2 + CH_3CHO PES given in Figure 7.

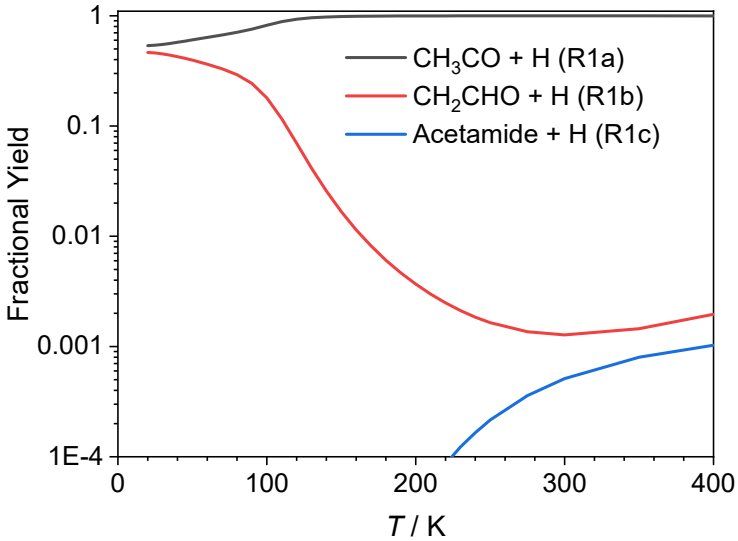

Figure S12. Reduced potential energy surface used for the fitting of experimental data, and calculating the rate coefficients given in Figure Sxxx by MESMER.

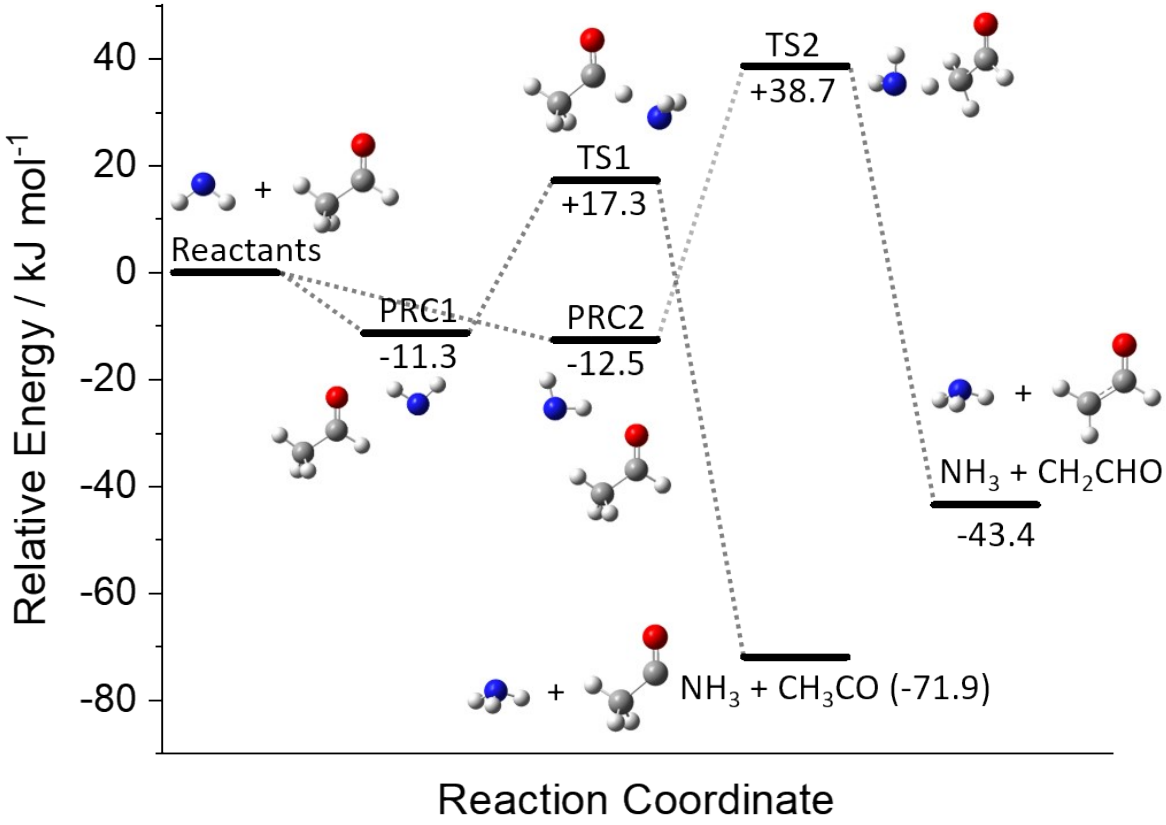

Figure S13. Experimental and theoretical rate coefficients for reaction R1. The theoretical rate coefficients predicted by MESMER were carried out using the reduced PES shown in Figure S9, with Ar as the third body at 1×10^{17} molecule cm^{-3}. The red diamonds give the results from a vibration only calculation, while the blue triangles give the results when hindered rotors are included in the calculation, which changes the density of states. Black circles are the experimental results collected in Ar bath gas in this study (those collected at ~ 1×10^{17} molecule cm^{-3}), while the solid green line is the experimental results from [28] (ref xxx).

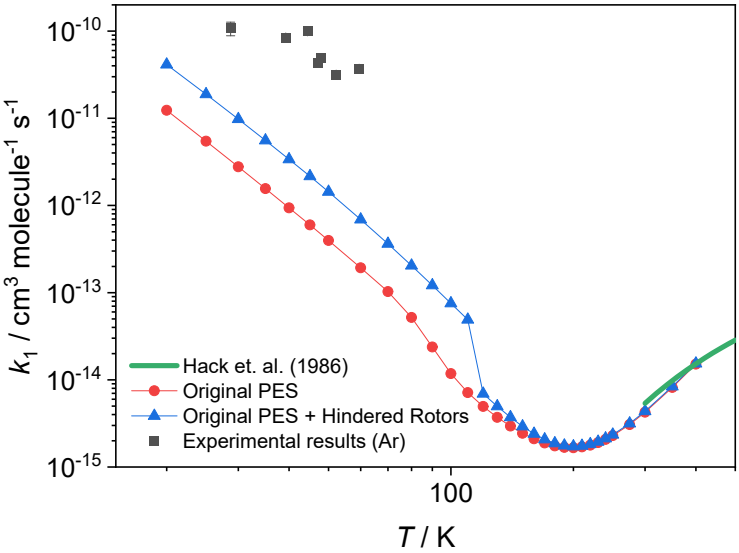

Figure S14. Internal rotations in CH_3CHO, PRC1, PRC2, TS1, TS2, and CH3CO that are described with the hindered rotor approach.

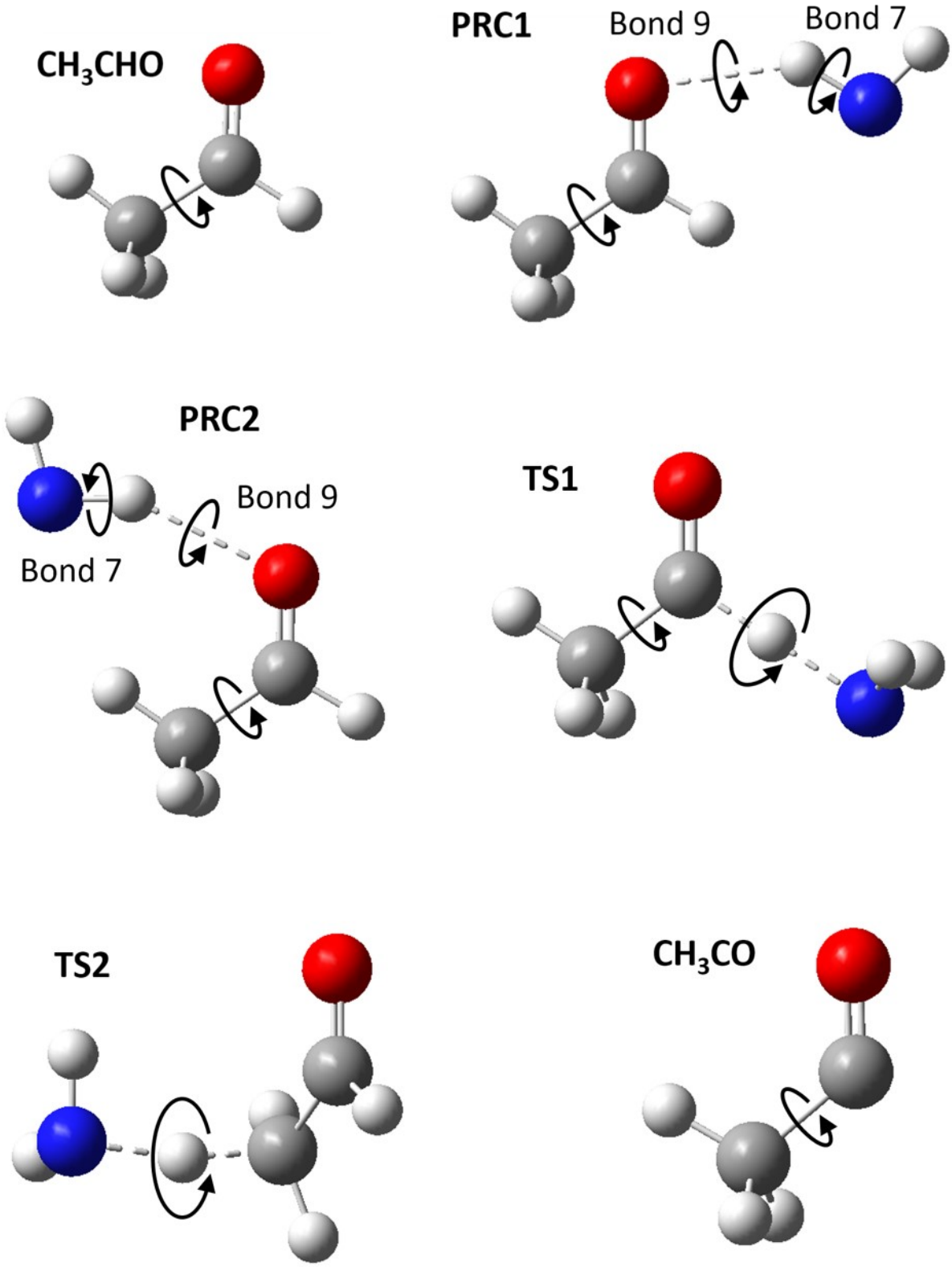

Table S15. Comparison of the calculated rate coefficients to the experimental values following fitting of the ZPEs of the PRCs to the experimental data.

Bath Gas	Temperature / K	Density / molecule cm^{-1}	Rate coefficient / cm^3 $molecule^{-1}$ s^{-1}		% Difference
			Experiment	Calculation	
N_2	70.0	1.38E+16	2.54E-12	1.94E-12	24 %
	67.1	2.50E+16	8.39E-12	3.78E-12	55 %
	67.1	2.50E+16	1.53E-11	3.78E-12	75 %
	64.6	4.50E+16	9.21E-12	7.05E-12	23 %
	62.9	6.41E+16	2.80E-11	1.02E-11	63 %
	89.9	4.19E+16	7.17E-12	1.93E-12	73 %
	84.4	7.40E+16	5.67E-12	4.01E-12	29 %
	80.5	1.30E+17	2.57E-11	7.63E-12	70 %
	78.4	1.77E+17	1.43E-11	1.08E-11	25 %
	92.9	5.28E+16	1.71E-12	2.07E-12	21 %
	87.4	9.12E+16	9.24E-12	4.19E-12	55 %
	85.6	1.27E+17	1.14E-11	5.97E-12	48 %
	106.7	7.55E+16	4.24E-12	1.63E-12	62 %
	99.5	1.27E+17	2.07E-12	3.38E-12	63 %
	97.0	1.77E+17	2.11E-12	4.94E-12	134 %
Ar	34.2	2.06E+16	3.77E-11	3.09E-11	18 %
	30.3	3.41E+16	5.82E-11	6.28E-11	8 %
	28.7	6.17E+16	1.08E-10	1.06E-10	2 %
	52.2	6.22E+16	3.17E-11	1.72E-11	46 %
	47.0	1.12E+17	4.37E-11	3.72E-11	15 %
	39.3	1.65E+17	8.46E-11	8.17E-11	3 %
	41.6	2.82E+17	9.88E-11	9.70E-11	2 %
	47.9	6.24E+16	4.89E-11	2.30E-11	53 %
	44.4	1.12E+17	9.95E-11	4.43E-11	55 %
	43.3	1.59E+17	1.16E-10	6.04E-11	48 %
	59.4	8.82E+16	3.70E-11	1.44E-11	61 %
	54.2	1.50E+17	6.28E-11	2.93E-11	53 %
	52.4	2.05E+17	9.69E-11	4.05E-11	58 %
He	42.2	2.58E+16	1.74E-11	1.45E-11	16 %
	37.2	4.58E+16	3.56E-11	3.37E-11	5 %
	35.0	6.13E+16	3.69E-11	5.02E-11	36 %
	34.3	8.79E+16	4.72E-11	6.72E-11	42 %
	55.4	1.00E+17	1.76E-11	1.56E-11	11 %
	55.4	1.00E+17	1.56E-11	1.56E-11	0 %
	50.9	1.79E+17	3.48E-11	3.19E-11	8 %
	47.6	2.35E+17	3.89E-11	4.76E-11	22 %
	54.6	7.44E+16	1.40E-11	1.31E-11	6 %
	51.8	1.01E+17	2.30E-11	1.98E-11	14 %
	49.6	1.40E+17	3.13E-11	2.91E-11	7 %
	63.2	6.83E+16	7.97E-12	7.20E-12	10 %
	62.9	1.35E+17	7.28E-12	1.26E-11	72 %
	60.0	1.86E+17	1.61E-11	1.89E-11	17 %

Table S16. Comparison of the calculated instant CH_3CO yields to the experimental values following fitting of the ZPEs of the H-abstraction TSs (TS1 and TS2) to the experimental data.

Bath Gas	Temperature / K	Density / molecule cm^{-1}	Instant CH_3CO yield		% Difference
			Experiment	Calculation	
N_2	67	2.5E+16	0.029	0.03050	5 %
He	37	4.6E+16	0.026	0.02557	2 %

Figure S17. Temperature and pressure dependent rate coefficients for the reaction between NH_2 + CH_3CHO (R1), as calculated by MESMER, using the PRC and TS energies determined by fitting to the experimental data, and Ar as the bath gas. It should be noted that the high- and low-pressure limiting rates will not be affected by the bath gas, however those in the pressure dependent region will be.

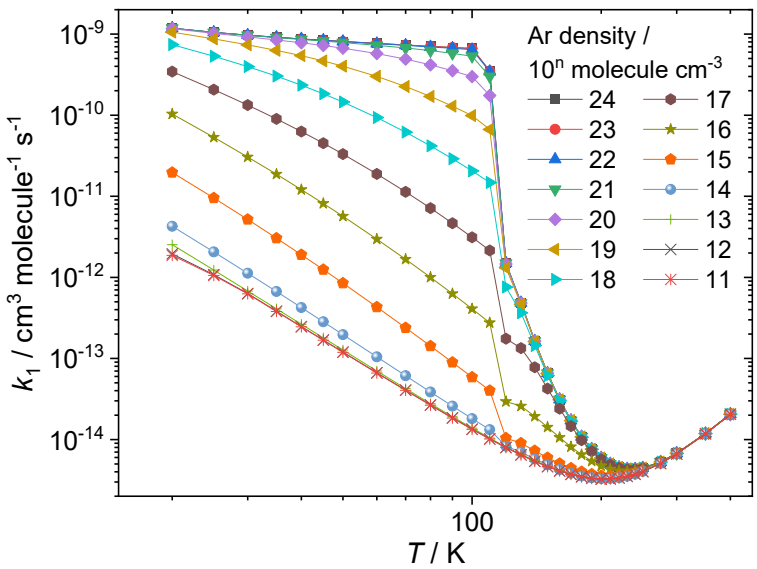

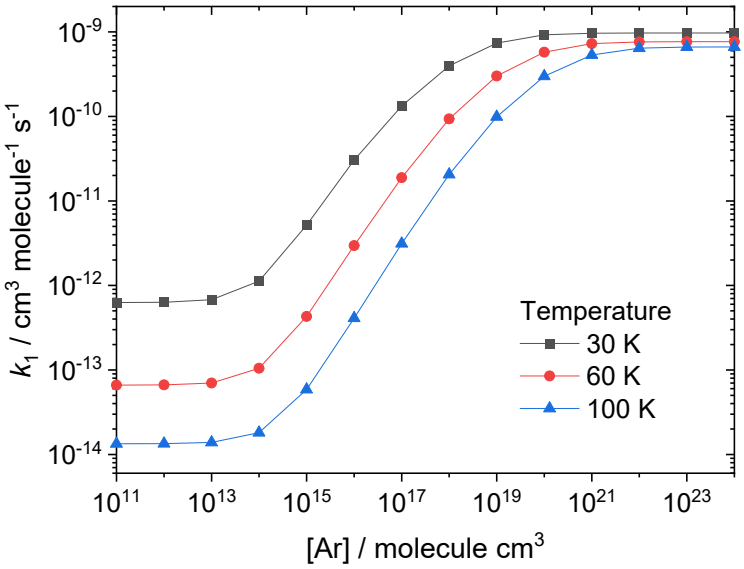

References.

1. Saladino, R.; Crestini, C.; Pino, S.; Costanzo, G.; Di Mauro, E. *Phys. Life Rev.,*2012, **9,** 84-104.
2. Rubin, R. H.; Swenson, G. W.; Benson, R. C.; Tigelaar, H. L.; Flygare, W. H. *Astrophysical Journal,*1971, **169,** L39-&.
3. Hollis, J. M.; Lovas, F. J.; Remijan, A. J.; Jewell, P. R.; Ilyushin, V. V.; Kleiner, I. *Astrophys. J.,*2006, **643,** L25-L28.
4. Herbst, E.;van Dishoeck, E. F., Complex Organic Interstellar Molecules. In *Annual Review of Astronomy and Astrophysics, Vol 47*, Blandford, R.; Kormendy, J.; VanDishoeck, E., Eds. 2009; Vol. 47, pp 427-480.
5. McGuire, B. A. *Astrophys. J. Suppl. Ser.,*2022, **259,** 30.
6. Vasyunin, A. I.;Herbst, E. *Astrophys. J.,*2013, **769,** 9.
7. Heard, D. E. *Acc. Chem. Res.,*2018, **51,** 2620-2627.
8. Shannon, R. J.; Blitz, M. A.; Goddard, A.; Heard, D. E. *Nat. Chem.,*2013, **5,** 745-749.
9. Antinolo, M.; Agundez, M.; Jimenez, E.; Ballesteros, B.; Canosa, A.; El Dib, G.; Albaladejo, J.; Cernicharo, J. *Astrophys. J.,*2016, **823**.
10. Canosa, A. *Proc. Int. Astron. Union,*2019, **15,** 35-40.
11. Gomez Martin, J. C.; Caravan, R. L.; Blitz, M. A.; Heard, D. E.; Plane, J. M. C. *J. Phys. Chem. A,*2014, **118,** 2693-2701.
12. Ocana, A. J.; Blazquez, S.; Potapov, A.; Ballesteros, B.; Canosa, A.; Antinolo, M.; Vereecken, L.; Albaladejo, J.; Jimenez, E. *Phys. Chem. Chem. Phys.,*2019, **21,** 6942-6957.
13. Nguyen, T. L.; Ruscic, B.; Stanton, J. F. *J. Chem. Phys.,*2019, **150**.
14. Roncero, O.; Zanchet, A.; Aguado, A. *Phys. Chem. Chem. Phys.,*2018, **20,** 25951-25958.
15. Shannon, R. J.; Caravan, R. L.; Blitz, M. A.; Heard, D. E. *Phys. Chem. Chem. Phys.,*2014, **16,** 3466-3478.

16. Acharyya, K.; Herbst, E.; Caravan, R. L.; Shannon, R. J.; Blitz, M. A.; Heard, D. E. *Mol. Phys.,*2015, **113,** 2243-2254.

17. Sandford, S. A.; Nuevo, M.; Bera, P. P.; Lee, T. J. *Chem. Rev.,*2020, **120,** 4616-4659.

18. Altwegg, K.; Balsiger, H.; Bar-Nun, A.; Berthelier, J. J.; Bieler, A.; Bochsler, P.; Briois, C.; Calmonte, U.; Combi, M. R.; Cottin, H., et al. *Sci. Adv.,*2016, **2**.

19. Douglas, K. M.; Lucas, D. I.; Walsh, C.; West, N. A.; Blitz, M. A.; Heard, D. E. *Astrophys. J. Lett.,*2022, **937**.

20. Barone, V.; Latouche, C.; Skouteris, D.; Vazart, F.; Balucani, N.; Ceccarelli, C.; Lefloch, B. *Mon. Not. R. Astron. Sco.,*2015, **453,** L31-L35.

21. Skouteris, D.; Vazart, F.; Ceccarelli, C.; Balucani, N.; Puzzarini, C.; Barone, V. *Mon. Not. R. Astron. Sco.,*2017, **468,** L1-L5.

22. Vazart, F.; Calderini, D.; Puzzarini, C.; Skouteris, D.; Barone, V. *J. Chem. Theory Comput.,*2016, **12,** 5385-5397.

23. Song, L.;Kästner, J. *Phys. Chem. Chem. Phys.,*2016, **18,** 29278-29285.

24. Halfen, D. T.; Ilyushin, V.; Ziurys, L. M. *Astrophys. J.,*2011, **743**.

25. Altwegg, K.; Balsiger, H.; Berthelier, J. J.; Bieler, A.; Calmonte, U.; Fuselier, S. A.; Goesmann, F.; Gasc, S.; Gombosi, T. I.; Le Roy, L., et al. *Mon. Not. R. Astron. Sco.,*2017, **469,** S130-S141.

26. Goesmann, F.; Rosenbauer, H.; Bredehoft, J. H.; Cabane, M.; Ehrenfreund, P.; Gautier, T.; Giri, C.; Kruger, H.; Le Roy, L.; MacDermott, A. J., et al. *Sci.,*2015, **349,** aab0689.

27. Foo, L.; Suranyi, A.; Guljas, A.; Szori, M.; Villar, J. J.; Viskolcz, B.; Csizmadia, I. G.; Ragyanszki, A.; Fiser, B. *Mol. Astrophys.,*2018, **13,** 1-5.

28. Hack, W.; Kurzke, H.; Rouveirolles, P.; Wagner, H. G. *Ber. Bunsen Ges. Phys. Chem.,*1986, **90,** 1210-1219.

29. Taylor, S. E.; Goddard, A.; Blitz, M. A.; Cleary, P. A.; Heard, D. E. *Phys. Chem. Chem. Phys.,*2008, **10,** 422-437.

30. Caravan, R. L.; Shannon, R. J.; Lewis, T.; Blitz, M. A.; Heard, D. E. *J. Phys. Chem. A,*2015, **119,** 7130-7137.

31. Douglas, K.; Blitz, M. A.; Feng, W. H.; Heard, D. E.; Plane, J. M. C.; Slater, E.; Willacy, K.; Seakins, P. W. *Icarus,*2018, **303,** 10-21.

32. Douglas, K. M.; Blitz, M. A.; Feng, W.; Heard, D. E.; Plane, J. M. C.; Rashid, H.; Seakins, P. W. *Icarus,*2019, **321,** 752-766.

33. West, N. A.; Millar, T. J.; Van de Sande, M.; Rutter, E.; Blitz, M. A.; Decin, L.; Heard, D. E. *Astrophys. J.,*2019, **885,** 134.

34. Bull, S.; Seregrennaja, I.; Tsherbakora, P. *Khim. Prom.(Moscow),*1963, **7,** 507-509.

35. Keller-Rudek, H.; Moortgat, G. K.; Sander, R.; Sörensen, R. *Earth Syst. Sci. Data,*2013, **5,** 365-373.

36. Copeland, R. A.; Crosley, D. R.; Smith, G. P. In *Laser-induced fluorescence spectroscopy of NCO and NH2 in atmospheric pressure flames*, Symposium (International) on Combustion, Elsevier: 1985; pp 1195-1203.

37. Donnelly, V. M.; Baronavski, A. P.; McDonald, J. R. *Chem. Phys.,*1979, **43,** 271-281.

38. Yamasaki, K.; Watanabe, A.; Kakuda, T.; Itakura, A.; Fukushima, H.; Endo, M.; Maruyama, C.; Tokue, I. *J. Phys. Chem. A,*2002, **106,** 7728-7735.

39. Limão-Vieira, P.; Eden, S.; Mason, N. J.; Hoffmann, S. V. *Chem. Phys. Lett.,*2003, **376,** 737-747.